Journal of Applied Physics

RESEARCH ARTICLE | FEBRUARY 26 2026

Excimer-laser-annealing-induced crystallization and atomic ordering of Co$_2$Mn$_{0.5}$Fe$_{0.5}$Ge Heusler alloy thin films for spintronic applications

Hirofumi Suto ; Keita Katayama ; Yohei Tanaka; Dolly Taparia; Nattamon Suwannaharn ;
Tomoya Nakatani ; Taisuke T. Sasaki ; Hisato Yabuta ; Yuya Sakuraba

J. Appl. Phys. 139, 083903 (2026)
https://doi.org/10.1063/5.0304815

AIP Publishing

Journal of
Applied Physics

ARTICLE

pubs.aip.org/aip/jap

Excimer-laser-annealing-induced crystallization and atomic ordering of $Co_2Mn_{0.5}Fe_{0.5}Ge$ Heusler alloy thin films for spintronic applications

Cite as: J. Appl. Phys. **139**, 083903 (2026); doi: 10.1063/5.0304815
Submitted: 30 September 2025 · Accepted: 14 January 2026 ·
Published Online: 26 February 2026

View Online Export Citation CrossMark

Hirofumi Suto,[1,a)] Keita Katayama,[2,3] Yohei Tanaka,[3] Dolly Taparia,[1] Nattamon Suwannaharn,[1] Tomoya Nakatani,[1] Taisuke T. Sasaki,[1] Hisato Yabuta,[2,3] and Yuya Sakuraba[1]

AFFILIATIONS

[1] Research Center for Magnetic and Spintronic Materials, National Institute for Materials Science (NIMS), Tsukuba, Japan
[2] Graduate School of Information Science and Electrical Engineering, Kyushu University, Fukuoka, Japan
[3] Department of Gigaphoton Next GLP, Kyushu University, Fukuoka, Japan

[a)] **Author to whom correspondence should be addressed:** SUTO.Hirofumi@nims.go.jp

ABSTRACT

Magnetic Heusler alloys are highly attractive for spintronics; however, realizing their full potential requires high-temperature annealing, which is often incompatible with practical device fabrication. Excimer laser annealing (ELA) potentially addresses this temperature constraint by making use of the short annealing time and temperature gradient along the depth direction. We investigated the effect of ELA on $Co_2Mn_{0.5}Fe_{0.5}Ge$ half-metallic Heusler-alloy thin films and demonstrated that ELA successfully induces crystallization and *B*2 atomic ordering. Optimized ELA condition using low fluence with a high number of laser irradiations achieved reduced resistivity and negative anisotropic magnetoresistance, indicating improved atomic ordering and high spin polarization, while maintaining flatness of the films. These findings establish ELA as a viable annealing method for integrating high-performance Heusler alloys into the device structure with strict thermal budget. Moreover, ELA offers additional advantages such as enhanced throughput and selective area annealing, thereby broadening the scope of Heusler-alloy applications in spintronic devices.

I. INTRODUCTION

Heusler alloys exhibit intriguing properties such as high spin polarization found in Co-based half-metallic Heusler alloys, such as $Co_2Mn_{0.5}Fe_{0.5}Ge$ (CMFG),[1–6] $Co_2FeGa_{0.5}Ge_{0.5}$,[7–10] and others,[11,12] and a large anomalous Hall effect found in Co_2MnAl[13,14] and Co_2MnGa,[15,16] making them highly attractive materials for spintronic applications.[17,18] One major challenge in implementing Heusler-alloy-based thin film devices is the process temperature required to achieve their full potential for the following reason. In many Co-based Heusler alloys, denoted as Co_2YZ, the $L2_1$-ordered structure with atomic ordering in all the Co, *Y*, and *X* atoms is energetically most stable in thermal equilibrium. Deposited thin films, however, usually exhibit atomic disorder, leading to a *B*2 structure with disorder between *Y* and *Z* atoms, an *A*2 structure with disorder among all constituent atoms, or an amorphous structure. Such disorders are known to degrade the material properties, and annealing processes such as postdeposition furnace annealing or deposition at an elevated temperature are generally employed to promote atomic ordering. In the case of current-perpendicular-to-plane giant magnetoresistance (CPP-GMR) devices, the magnetoresistance (MR) ratio shows an increasing trend with respect to the process temperature up to 600 °C,[6] indicating the advantage of the improved atomic ordering at high process temperatures. However, practical applications impose temperature limitations. For example, in CPP-GMR read heads for hard-disk-drives, one of the most extensively studied spintronic applications of Heusler alloys, the process temperature is limited to 300 °C due to the temperature tolerance of the soft magnetic shield layers fabricated near the CPP-GMR device for improved spatial resolution.[17] Similarly, in the case of magnetoresistive random access memory, the process temperature of MR memory cells fabricated in the back-end-of-line process is limited to

400 °C.[19] In the case of spintronic devices on flexible substrates, temperature limitation ranges from 200–450 °C depending on the substrate materials. Currently, the implementation of the above applications is sought mainly by using conventional CoFe-based materials.[17,19–22] To address the above temperature constraint of Heusler alloys, research has been conducted to lower the required temperature through optimizing materials and structures. For example, the amorphization of CMFG by an amorphous seed layer[2,3] or alloying Co_2FeSi with a small amount of Ag[23,24] was reported effective to improve atomic ordering at relatively low annealing temperatures. In addition, annealing Heusler-based films at sufficient temperature on a high-temperature compatible structure followed by transferring and bonding to the device structure has been studied.[25]

Excimer laser annealing (ELA) is an alternative annealing method that can overcome the temperature constraints. In ELA, pulsed laser is applied to the sample to induce an annealing effect. Because of the short pulse width typically in the nanosecond region, ELA can prevent the sample from sustained exposure to high temperature. Furthermore, laser absorption and heat generation occur primarily near the surface, creating a temperature gradient along the depth direction. Therefore, by optimizing the laser condition and thermal design of devices, conducting ELA right after the deposition of Heusler-based device films can allow the films to reach a sufficient temperature, while keeping the underlying structures cooler than the temperature limitation. ELA has been extensively studied for the fabrication of low-temperature polysilicon thin films on glass or flexible substrates, where amorphous Si layers are rapidly heated to the melting point for crystallization before heat diffusion into the substrate causes damage.[26–28] Moreover, the ELA application has been explored for a wide variety of functional materials, with motivations such as integrating the materials into devices with low thermal budget or increasing heating and cooling rates.[29–34] Laser annealing also offers the advantage of selected-area annealing by defining the irradiated area.[34] This selected-area annealing enables the local control of magnetization direction of the pinned layer in spin-valve MR devices.[35–37] However, the use of ELA in ordered alloys such as Heusler alloys remains unexplored.

In this study, we investigate the effect of ELA on sputter-deposited CMFG Heusler-alloy thin films for spintronic applications. Among half-metallic Co-based Heusler alloys, CMFG attracts attention owing to high atomic ordering obtained at relatively low annealing temperature. X-ray diffraction (XRD) measurements revealed that the CMFG film was amorphous in the as-deposited state and changed into a polycrystalline structure with *B*2 atomic ordering by ELA. The fluence required for crystallization decreases with increasing number of laser irradiation because the annealing effect is accumulated by multiple laser irradiations. An excess increase in fluence resulted in increased film roughness, being detrimental to practical applications. The effect of ELA was examined also by measuring anisotropic magnetoresistance (AMR) and resistivity. Based on the comparison of the AMR and resistivity between the samples treated with ELA and furnace annealing, ELA was found to induce the annealing effect equivalent to a temperature of 300 °C at which CMFG should show relatively good device performance. Transmission electron microscopy (TEM) observation shows the film after ELA has grain with a size of a few tens of nanometers without noticeable interdiffusion between seed and capping layers. These results demonstrate the potential of ELA as a viable annealing technique, broadening the scope of Heusler alloy applications.

II. EXPERIMENTAL

The samples were prepared by depositing Ta (2 nm)/$Co_{38}Fe_{38}B_{19}Ta_5$ (1.5 nm)/CMFG (50 nm)/Ru (2 nm) on 2 cm × 2 cm Si substrates with a 500 nm thermally oxidized layer by using magnetron sputtering. The order of the layers is from bottom to top. The composition of the CMFG layer was $Co_{49.7}Mn_{17.8}Fe_{9.3}Ge_{23.2}$, as measured by X-ray fluorescence analysis. ELA experiments were conducted using a KrF excimer laser (Gigaphoton Inc.) with a wavelength (λ) of 248 nm and a pulse duration of 83 ns by varying the following three ELA parameters: fluence, number, and frequency of laser pulses. The pulsed laser was introduced to homogenizing optics to form a uniform rectangular fluence profile with the area of $0.4 \times 1.2\ \text{mm}^2$ on the samples. This size of the irradiation area was chosen to allow the testing of various laser conditions within a single substrate and can be adjusted depending on the intended use in applications. The samples were placed in a chamber with constant Ar flow at the atmospheric pressure to suppress the oxidation of the samples, and the laser was introduced through the window of the chamber. By moving the sample chamber, laser irradiation was conducted on the designated position on the sample. Based on the complex refractive index of Ru used as the surface layer ($n = 1.05$ and $k = 2.75$), the reflectance at the surface defined by $((n-1)^2 + k^2)/((n+1)^2 + k^2)$ is calculated to be 0.64, and the penetration depth defined by $\lambda/4\pi k$ is calculated to be 7.2 nm. The penetration depth is larger than the Ru thickness, meaning that a substantial amount of laser penetrated into the CMFG layer. Although the detailed optical constant of CMFG is unknown, based on the fact that light penetration depth in metal in the UV region is typically 10 nm or shorter, the laser was mostly absorbed in the CMFG layer with little reaching the substrate. As a reference, the samples with a size of 10 × 10 mm were also processed with the conventional annealing in a vacuum furnace for 30 min at various post-annealing temperatures (T_p) from 200 to 500 °C. During furnace annealing, the temperature was ramped slowly from RT over the course of an hour to prevent overshoot.

Crystallization and atomic ordering were examined by XRD measurements (Rigaku SmartLab) with Cu-K_α radiation with a wavelength of 1.5406 Å. 2θ–ω scans were conducted using a two-dimensional detector (Rigaku HyPix-3000) with an active area of $77.5 \times 38.5\ \text{mm}^2$ placed at a camera length of 150 mm. The XRD profiles were obtained by integrating the ring pattern along the β angle using the whole two-dimensional images except for the 2θ range below 30° where the β range of 150°–210° was used. The β angle corresponds to the angle of the Debye ring with 180° being the perpendicular direction, and thus, the β angle dependence serves similar to the rocking curve measurement. The β range of 179°–181° was excluded in the profiles to get rid of the strong substrate peaks with Si 004 appearing approximately at 69°. The Si 004 peaks also appeared at 66° and 62° due to Cu-K_β and W-L_α energies contained in the source x ray, respectively, and the forbidden Si 002 peak sometimes appeared at 33° due to multiple reflections. Surface morphology was measured by atomic force microscopy

(AFM) with a scan area of $1 \times 1\,\mu\text{m}^2$ to estimate the average roughness (R_a). AMR and resistivity measurements were conducted by applying a current of 1 mA to the strips with a width of $40\,\mu$m and length of $170\,\mu$m and measuring the resistance by the four-terminal method. The strips were patterned by Ar ion milling after ELA or furnace annealing. AMR ratio is defined as $(\rho_{//}-\rho_{\perp})/\rho_{\perp}$, where $\rho_{//}$ and $\rho_{\perp}$ are the resistivity of films when the directions of the current and magnetic fields are parallel and orthogonal, respectively. According to theoretical and experimental studies, the cross-sectional scanning transmission electron microscopy (STEM) images, energy dispersive x-ray spectroscopy (EDS) elemental maps, selected-area electron diffraction (SAED), and nanobeam electron diffractions (NBED) were obtained for microstructure analysis utilizing FEI Titan G2 80-200 TEM operating at 200 kV.

III. RESULTS AND DISCUSSION

A. Effect of ELA and furnace annealing on crystallization, atomic ordering, and surface roughness

We first investigated the effect of conventional furnace annealing on the structure and morphology of the samples. Figure 1(a) shows the XRD profiles for as-deposited and furnace-anneal samples for $T_p = 200$–$500\,°$C. In the as-deposited state, a very broad peak at around $2\theta = 44°$ appears originating from short-range local atomic arrangements, which indicates the amorphous structure of the film without long-range order. After annealing at 200 °C, fundamental 004 and 202 peaks and a superlattice 002 peak appear, indicating that the CMFG layer changed to a poly-crystalline structure with $B2$ atomic ordering. No significant change in the XRD profiles was observed for $T_p = 200$–$500\,°$C. Figure 1(b) shows the 2D XRD images of the $T_p = 450\,°$C sample obtained for $\chi = 0°$ and 45°. For $\chi = 0°$, the ring patterns of 202 and 004 are observed, and the former shows a higher intensity at the upper and lower edges of the 2D image, whereas the latter shows a higher intensity near the center. On the other hand, only the 202 ring pattern is observed for $\chi = 45°$. This angle dependence of the peak intensities is summarized in the inset, where the center of the 004 peak appears in the perpendicular direction and that of the 202 peak is tilted by 45°, with the full width at half maximum of both peaks being approximately 30°. These results indicate a weak (001) texture of the CMFG film, with the {110} planes naturally tilted by 45° from the out-of-plane direction. The 002 peak is visible only in the profile and not in the 2D image due to its small intensity. According to the previous reports, $L2_1$ atomic ordering might exist at higher T_p, but the 111 superlattice peak reflecting the $L2_1$ ordering was not observed due to its small intensity. Note that all the furnace-anneal samples show good surface specularity, indicating their flat surface.

We next conducted ELA on the as-deposited sample. Figure 2(a) shows the photo image of the ELA sample for 10 Hz, 10 shots, and various fluences from 40 to 300 mJ/cm^2. The position marks were made by damaging the film with high fluence, denoted by the red box, and the 2 mm wide area next to the position mark is the ELA area made by sweeping the laser, denoted by the blue box. When the fluence is 200 mJ/cm^2 or more, the surface specularity was degraded, suggesting a change in the surface morphology. Figure 2(b) shows the corresponding XRD profiles. For fluence up to 100 mJ/cm^2, the profiles are the same as that of the as-deposited sample, indicating that the amorphous structure was unchanged. Above 120 mJ/cm^2, 004, 202, and 002 peaks appear, demonstrating that the crystallization and atomic ordering of the CMFG layers were successfully induced by ELA. At 260 mJ/cm^2, the peaks do not appear despite the visible change for unknown reasons. Figures 2(c) and 2(d) show the results from the same measurements when the shot number was increased to 1000. The degradation of surface specularity occurs from 160 mJ/cm^2, and severe damage was observed at 300 mJ/cm^2. XRD peaks appear from 100 mJ/cm^2. The peaks abruptly become sharp and intense from 200 mJ/cm^2. These strong peaks suggest the growth of larger grains by agglomeration, which can lead to the degradation of surface specularity. The fluence values at which the XRD peaks appeared

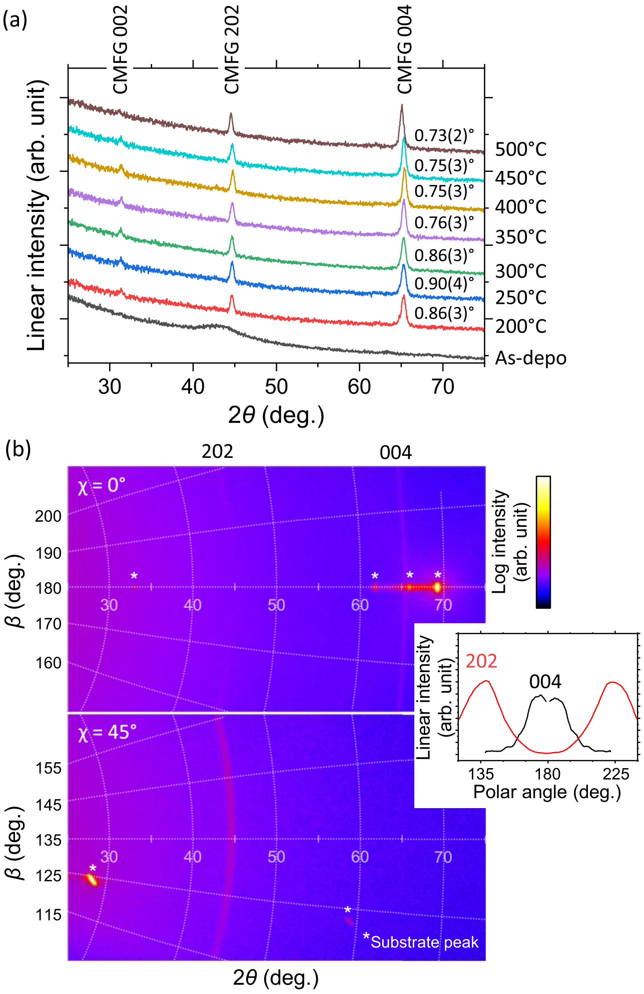

FIG. 1. (a) Out-of-plane XRD profiles obtained for the furnace-anneal samples at various post-annealing temperatures. Values shown to the right of the CMFG 004 peaks represent their integral width, with errors corresponding to the last digit of the main value indicated in parentheses. (b) 2D XRD image obtained at $T_p = 450\,°$C for $\chi = 0°$ (top) and 45° (bottom). The inset shows the polar angle profile of the peak intensities for 202 and 004 rings.

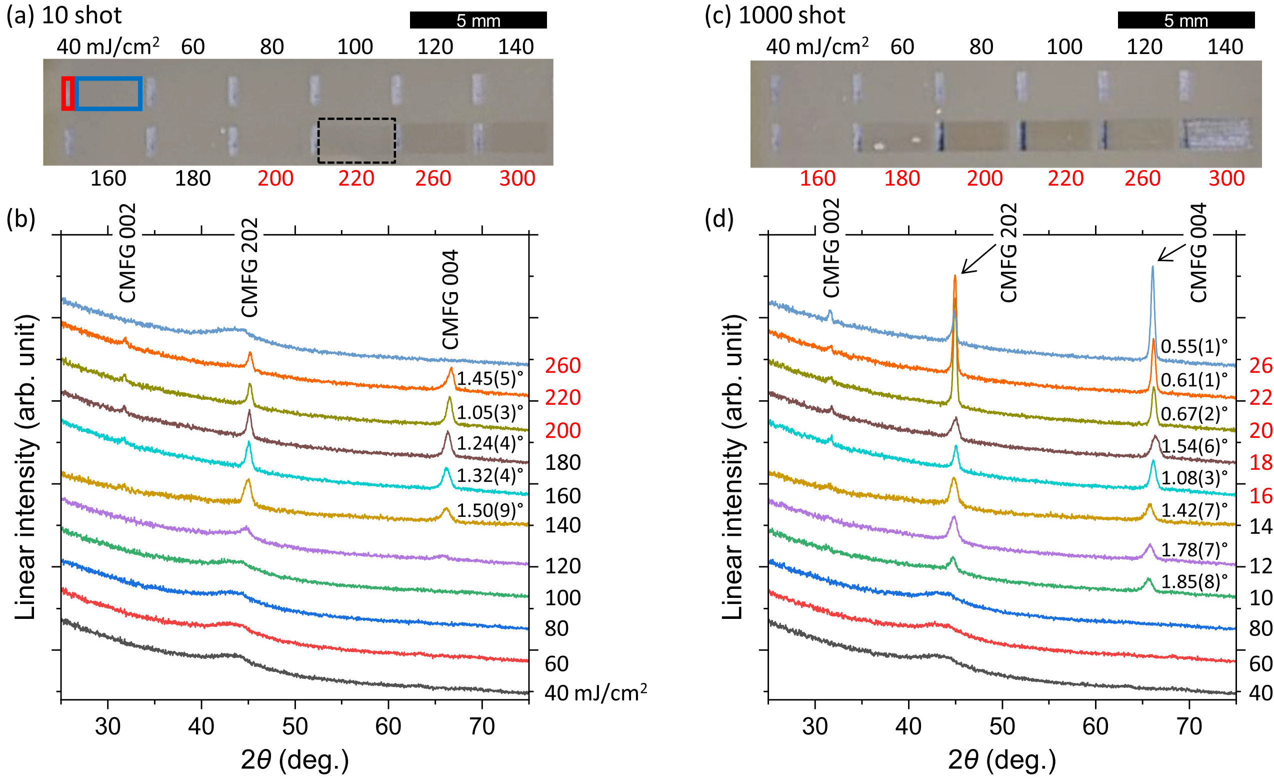

FIG. 2. (a) Photo image of the ELA sample for 10 Hz, 10 shots, and various fluences. The red square indicates the position mark made by strong laser, and the blue square indicates the ELA area for 40 mJ/cm^2. (b) Corresponding out-of-plane XRD profiles. Values shown to the right of the CMFG 004 peaks represent their integral width, with errors corresponding to the last digit of the main value indicated in parentheses. (c) and (d) Results from the same measurement for 10 Hz and 1000 shots. In (a), due to the experimental mistake, 220 mJ/cm^2 was conducted in a different position, and its image is copied as indicated by the black dashed square.

and the surface specularity degraded decreased by increasing the shot number from 10 to 1000, indicating these effects of ELA accumulate with a number of laser irradiations.

Figure 3(a) shows the out-of-plane lattice constants (*c*) as a function of T_p and fluence, evaluated from the 004 peak positions in the XRD results. In this analysis, the considered β angle range was reduced to 170°–179° and 181°–190° in determining the peak position to suppress the effect of change in lattice constants between the out-of-plane and in-plane directions, while maintaining a sufficient signal-to-noise ratio. The furnace-anneal sample shows the *c* values around 0.571 nm, which is slightly smaller than the reported bulk value of 0.574 nm. The ELA samples exhibit *c* values below 0.57 nm, which are smaller than the furnace-anneal sample, and exhibit a decreasing trend with fluence, suggesting that lattice strain is induced in the ELA samples, presumably due to much faster rate of temperature change. To evaluate the strain, the in-plane lattice constant (*a*) of the furnace-anneal ($T_p = 450\,°C$) sample was calculated from the *c* value and the 202 peak position at $\chi = 45°$ with the β angle range of 130°–140°, yielding $a = 0.578$ nm. For further confirmation, in-plane grazing-incidence XRD with an incidence angle of 0.4° was also conducted to measure the 400 peak position (data not shown), yielding $a = 0.58$ nm. These two *a* values are consistent and slightly larger than the *c* value, and the *c*/*a* ratio is estimated to be 0.98–0.99. Similarly, the *a* value was evaluated to be 0.584 nm for the ELA sample (10 shots and 180 mJ/cm^2) using the two XRD scans at $\chi = 0$ and 45°. In-plane grazing-incidence XRD could not be performed due to the small ELA area. The *c*/*a* ratio is estimated to be 0.96, confirming that ELA induces larger strain than furnace annealing. The fluence dependence of the lattice constant changes the trend at 200 mJ/cm^2 for 1000 shots, which can be attributed to the relaxation of the lattice strain by agglomeration.

The integral width of the 004 peaks was also evaluated, as shown in Figs. 1(a), 2(b), and 2(d). The furnace-anneal samples exhibit width in the range of 0.7°–0.9°. The ELA samples generally show a broader linewidth than the furnace-anneal samples, except for high-fluence region above 200 mJ/cm^2 for 1000 shots. The broader linewidth indicates that the ELA samples have a smaller crystallite size, larger lattice strain, and/or higher number of defects. In the high fluence range for 1000 shots, the linewidth decreases, suggesting that increased atomic diffusion by high-fluence laser resulted in strain relaxation and formation of larger grains. In addition, for 220 mJ/cm^2 for 10 shots, where the *a* value shows the minimum among all the samples, the 004 peak exhibits

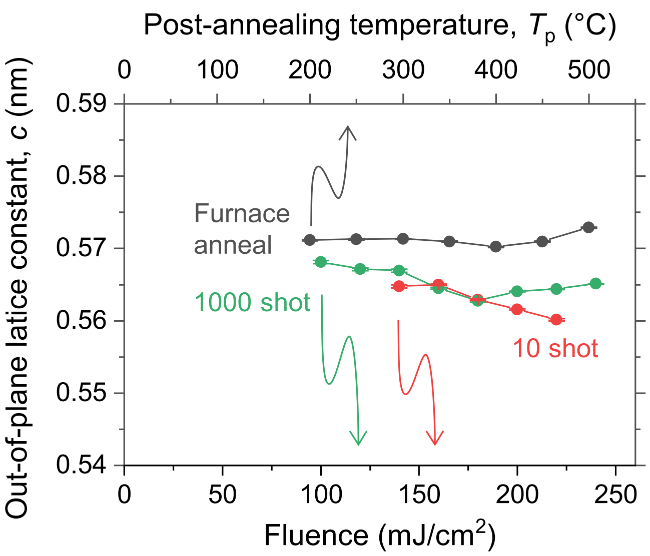

FIG. 3. T_p dependence of c for the furnace-anneal samples and fluence dependence of c for the ELA samples.

an asymmetric shape with a tail to the lower angle, suggesting strain-related defects.

AFM observations were conducted to quantitatively evaluate the surface roughness. Figure 4 shows the fluence dependence of R_a for 10 and 1000 shots, and the inset shows the T_p dependence of R_a of the furnace-anneal samples. In the as-deposited state, the sample surface is very flat with an R_a of approximately 0.15 nm. For furnace annealing, the roughness increases slightly with T_p to approximately 0.4 nm at $T_p = 500\,°C$. For ELA, the roughness remains unchanged up to 140 mJ/cm^2 and starts to increase, and the increase is higher for 1000 shots due to the accumulated effect from multiple laser irradiations. The ELA conditions with increased roughness show overall agreement with the visible change of the samples in Figs. 2(a) and 2(c), indicating that the degraded surface specularity arose from the roughness. Increased roughness can be detrimental in practical applications, especially for MR devices

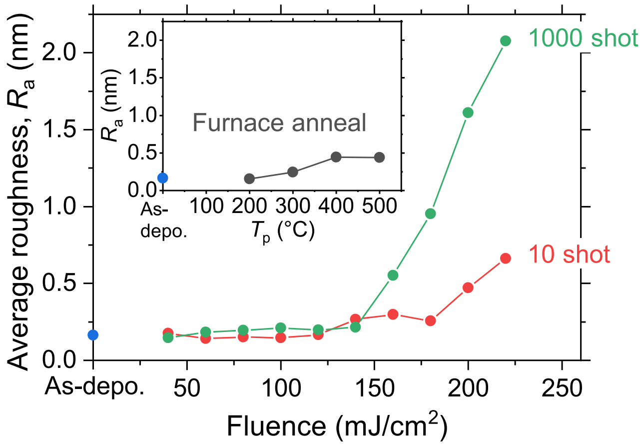

FIG. 4. Fluence dependence of R_a for 10 and 1000 shots (10 Hz) for the ELA samples. The inset shows the T_p dependence of R_a for the furnace-anneal samples.

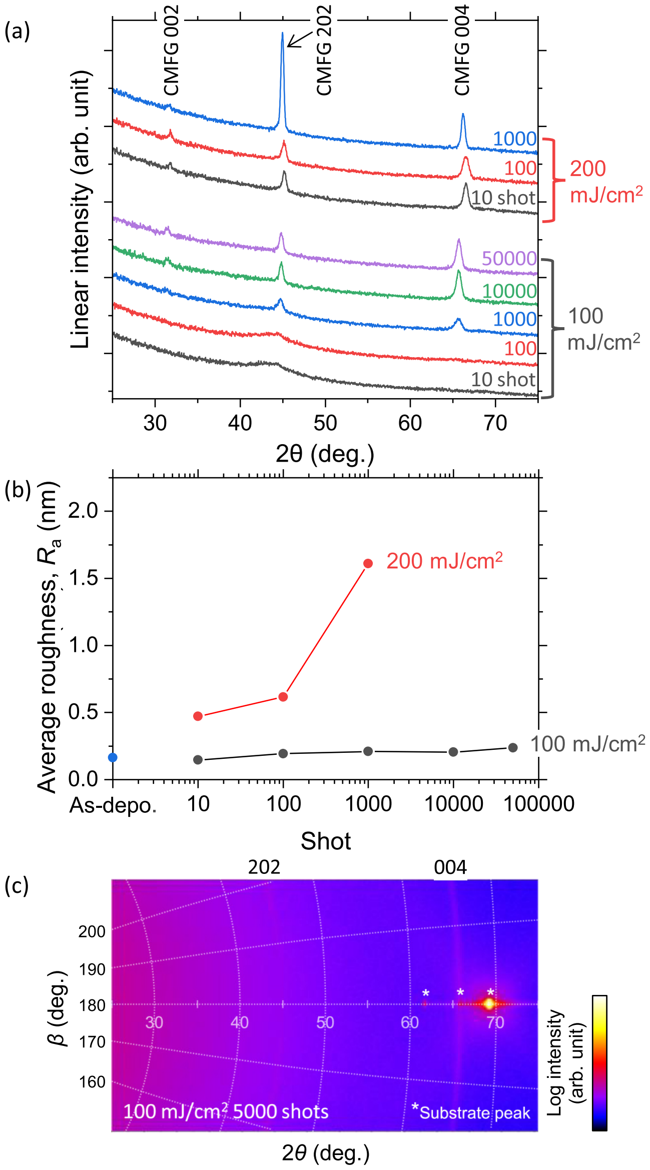

FIG. 5. (a) Out-of-plane XRD profiles obtained for the ELA samples for various shot number for 100 and 200 mJ/cm^2. The irradiation frequency was 10 Hz for 10, 100, and 1000 shots, and 1000 Hz for 10000 and 50000 shots. Shot number dependence of R_a for 100 and 200 mJ/cm^2. (c) 2D XRD image for 100 mJ/cm^2 and 50 000 shots (1000 Hz).

consisting of stacked nanometer-scale multilayers, where interface quality is crucial to the device performance.

The effect of shot number is examined by extending its upper range to 50 000. Figures 5(a) and 5(b) show the dependence of the XRD profiles on the shot number and the corresponding R_a, respectively. Frequency of laser irradiation was set to 10 Hz for 10, 100, and 1000 shots and 1000 Hz for 10 000 and 50 000 shots. For 200 mJ/cm^2, XRD peaks already appear for ten shots and intensify with the shot number, which accompanies with an increase in the roughness. On the other hand, for 100 mJ/cm^2, the peaks appear first for 1000 shots and intensify with the shot number, which caused no roughness increase even at 50 000 shots. These results indicate that, by limiting the fluence below a certain threshold, crystallization and atomic ordering can be promoted by repeating the laser irradiation without affecting the roughness. Figure 5(c) shows the 2D XRD image obtained for 100 mJ/cm^2 and 50 000 shots, which exhibit the ring patterns of 004 and 202 similar to that of the furnace-anneal sample.

B. Effect of ELA and furnace annealing on resistivity and AMR

We next investigate the effect of furnace annealing and ELA on the electrical and magneto-transport properties. Figures 6(a) and 6(b) show the T_p dependence of the resistivity and AMR ratio for as-deposited and furnace-anneal samples, respectively. Both resistivity and AMR ratio decrease monotonically with T_p up to 450 °C. By further increasing T_p to 500 °C, the resistivity increases, whereas the AMR ratio continues to decrease. Resistivity generally reflects the film structure, grain size, and atomic ordering.[38] Considering that the surface flatness was maintained in the furnace-anneal samples, the decrease in resistivity is likely due to the promoted grain growth, reduced defects, and improved atomic ordering induced by annealing. Consistent with this interpretation, the linewidth of the XRD peaks in Fig. 1(a) shows overall narrowing trend with T_p. With regard to the AMR effect, its physical origin has been theoretically understood by considering *s–d* scattering of conduction electrons.[39] In particular, the model developed

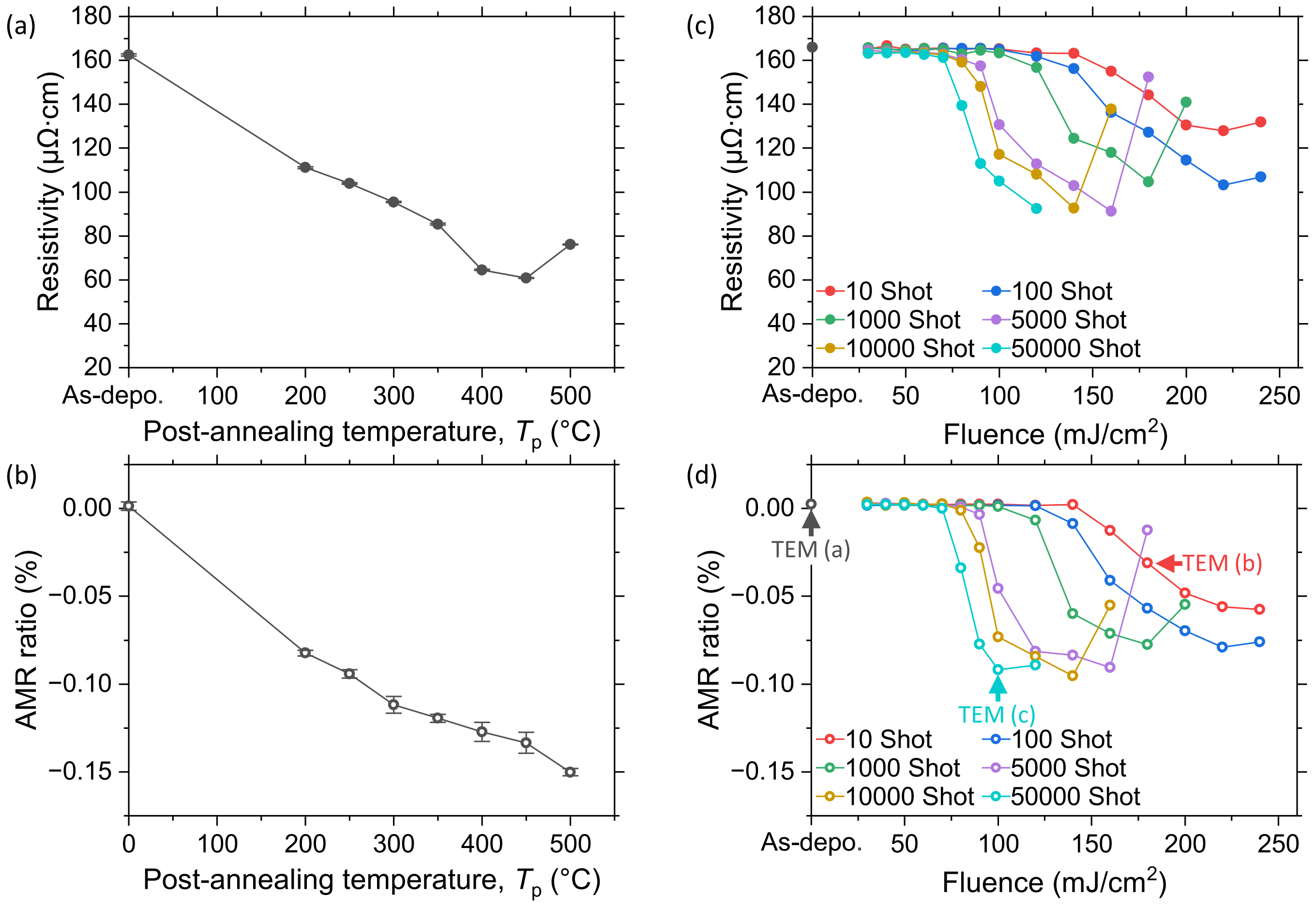

FIG. 6. T_p dependence of (a) resistivity and (b) AMR ratio obtained for the furnace-anneal samples. Fluence dependence of (c) resistivity and (d) AMR ratio obtained for the ELA samples with different shot numbers. Arrows show the conditions for samples used in TEM observation.

by Kokado *et al.* predicts half-metallic materials to exhibit negative AMR, originating from the dominant s–d scattering of $s\uparrow \rightarrow d\uparrow$ or $s\downarrow \rightarrow d\downarrow$.[40] This model has been experimentally validated in a variety of Co-based Heusler alloys, where the magnitude of negative AMR correlates with half-metallicity.[41–43] Based on these previous findings, enhanced negative AMR observed at higher T_p can be attributed to improved half-metallicity as a result of improved atomic ordering. Despite the indication of improved atomic ordering from the above discussion, the 002 superlattice peak XRD results in Fig. 1(a) show little T_p dependence because XRD is insensitive to change in the atomic ordering among atoms with close atomic numbers such as Co, Fe, and Mn.

Figures 6(c) and 6(d) show the fluence dependence of the resistivity and AMR ratio for the ELA samples with different shot numbers, respectively. The frequency of laser irradiation was set to 10 Hz for 10, 100, and 1000 shots and 1000 Hz for 5000, 10 000, and 50 000 shots. As will be discussed in detail later, changing frequency from 10 to 1000 Hz affects the results due to increased heat accumulation by fast repetition of laser irradiation. However, the overall trend remains unchanged, and the fluence shift originating from heat accumulation is typically around 50 mJ/cm^2, confirming that frequency does not affect the interpretation of data in Figs. 6(c) and 6(d). Assuming all measurements were conducted at the same frequency, the gap of the results for 1000 and 5000 shots would shrink. In the case of ten shots, the resistivity is unchanged up to 140 mJ/cm^2, gradually decreases to the minimum at 220 mJ/cm^2, and then slightly increases. The AMR ratio exhibits a similar trend. Notably, the onset of resistivity reduction and negative AMR at 160 mJ/cm^2 coincides with the emergence of XRD peaks, indicating that the decreases in resistivity and the enhancement in negative AMR originate from the promoted crystallization and atomic ordering due to ELA. In the fluence range where the resistance decreases and the negative AMR enhances, the XRD peak width shows an overall narrowing trend, supporting that these changes partly originate from the grain growth and reduced defects. An increase in resistivity after reaching the minimum can be attributed to increased surface roughness, as supported by the AFM results. In addition, interdiffusion among the layers may also contribute to the resistivity increase. Regarding the horizontal axis, the position of both the onset of the resistivity change and the minimum resistivity shifts to the lower fluence side with the shot number. Regarding the vertical axis, the minimum resistivity decreased with the shot number, achieving 92 $\mu\Omega$ cm for 10 000 and 50 000 shots and the fluence range of 100–140 mJ/cm^2. The trend in the AMR ratio follows that of the resistivity, with the largest negative AMR ratio being −0.095%. Notably, this fluence range does not affect the roughness.

Comparison between ELA and furnace annealing results reveals that the minimum resistivity achieved by ELA corresponds to the values obtained at furnace annealing temperatures between 300 and 350 °C. Similarly, the maximum negative AMR ratio by ELA corresponds to values between 250 and 300 °C, indicating that the effect of ELA is equivalent to annealing at approximately 300 °C. However, the minimum resistivity and largest negative AMR of the ELA samples under the tested conditions could not reach those of the furnace-anneal samples at higher T_p, indicating that the furnace annealing at higher T_p can achieve higher atomic ordering and half-metallicity than ELA. Nevertheless, the studies on CPP-GMR devices with CMFG reported that furnace annealing at 300 °C exhibited relatively good MR output, due to the improved $B2$ ordering.[3,5] Our findings suggest that CMFG films processed with the optimal ELA condition can potentially exhibit good device performance.

The total laser irradiation time for 50 000 shots is 4.15 ms (83 ns × 50 000 shots), and the total process time is 50 s (50 000 shots/1000 Hz). These times are remarkably shorter than that of the furnace annealing, which takes 30 min for the constant temperature along with the additional 2 h for heating and cooling the system, suggesting that the ELA can enhance the throughput of the annealing process.

We also investigated the effect of the frequency of laser irradiation. Figures 7(a) and 7(b) show the fluence dependence of resistivity and AMR ratio obtained for 1000 shot by setting the frequency to 10, 1000, and 2000 Hz and for 50 000 shots by setting the frequency to 1000 and 2000 Hz. In the case of 1000 shots, the

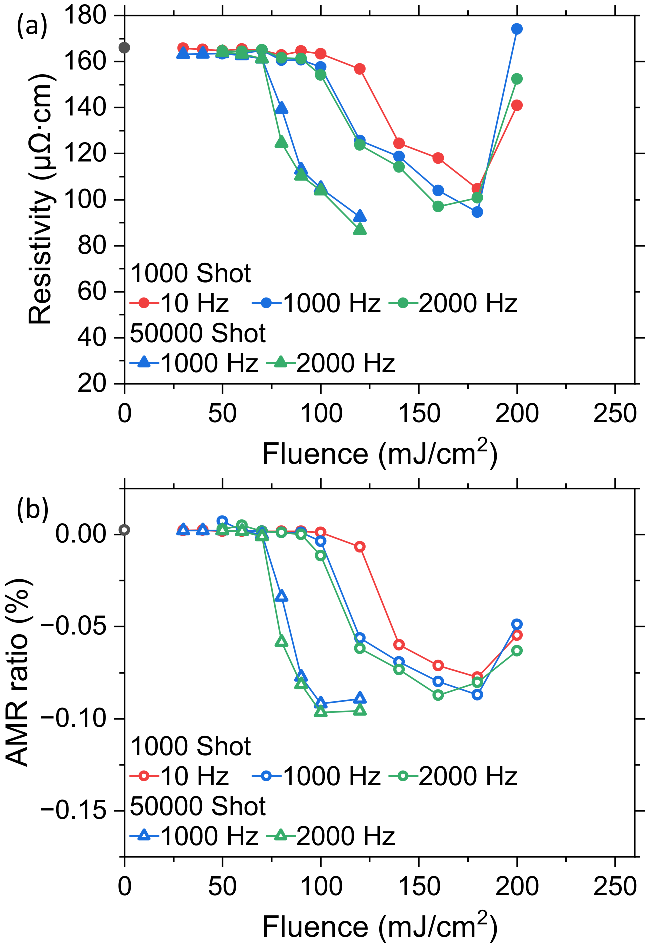

FIG. 7. Fluence dependence of (a) resistivity and (b) AMR ratio obtained for the ELA samples with different frequencies of laser irradiation.

onset of decrease in the resistivity and AMR shifts to the lower fluence side by increasing the frequency from 10 to 1000 Hz. This shift can be attributed to heat accumulation by repeated laser irradiation. As the interval between laser irradiation shortens with frequency, the heat from the prior laser irradiation remains, and the resultant temperature increase enhances the annealing effect. The results for 1000 and 2000 Hz also show a shift, although the shift is small, indicating that the temperature change by the residual heat is also small due to the small interval difference between 1000 and 2000 Hz.

C. Microstructure analysis by TEM

TEM analysis was conducted to investigate the microstructure and interface quality. Figures 8(a)–8(c) show the bright-field (BF) STEM images and their corresponding diffraction patterns for the as-deposited and two ELA samples with the following conditions: 10 shots, 10 Hz, 180 mJ/cm^2 and 50 000 shots, 1000 Hz, 100 mJ/cm^2. These two ELA conditions were selected to represent the lowest and highest shot numbers, while maintaining fluence below the threshold to affect surface roughness. The AMR results of these three TEM samples are marked by the arrows in Fig. 6(d) for ease of reference. The as-deposited sample exhibits no distinct grain boundaries, and the SAED acquired in the same area showed a clear halo feature superimposed with diffraction spots, which confirmed that the structure is mostly amorphous with some crystallization, consistent with the XRD results. In the ELA samples, crystalline grains were observed, and the SAED patterns exhibit rings of clear diffraction spots without a halo, indicating their polycrystalline nature and absence of an amorphous structure. Furthermore, the 002 superlattice spots confirm *B*2 atomic ordering in SAED or NBED taken from particular grains along [110] zone axis, consistent with the XRD results. The weak (001) texture observed in the XRD is not confirmed in the SAED patterns due to the low counting statistics of the grains. The structure of the Ta seed layer was amorphous regardless of the ELA condition (data not shown). Grain size varies depending on the laser conditions: the sample in (b) exhibits grains ranging from 20–40 nm, while the sample in (c) exhibits larger grains ranging from 30 to 60 nm. The sample in (b) was irradiated with

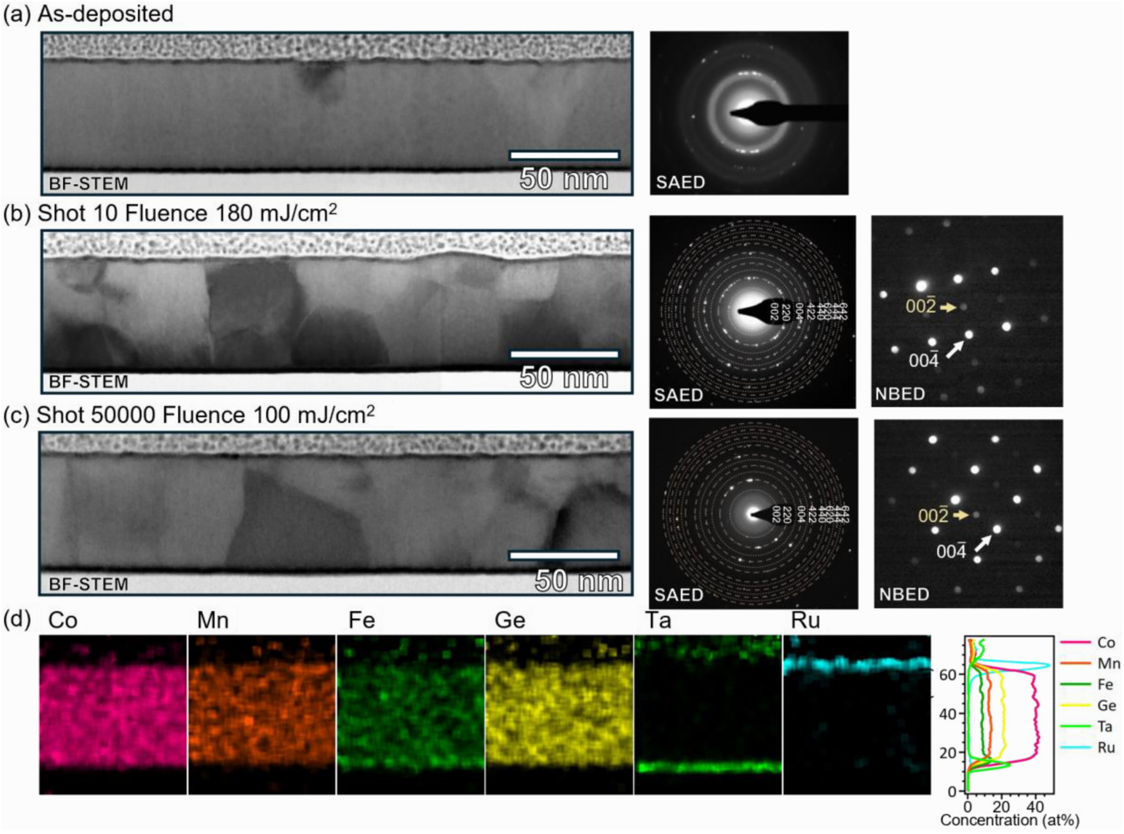

FIG. 8. Cross-sectional STEM images and electron diffraction patterns for (a) the as-deposited sample and the two ELA samples (b) 10 shots, 10 Hz, and 180 mJ/cm^2 and (c) 50 000 shots, 1000 Hz, and 100 mJ/cm^2. Dashed and dotted rings in the SAED patterns represent the positions of fundamental and *B*2 superlattice reflections, respectively. (d) EDS elemental map for the sample in (c) and corresponding compositional profile along the thickness direction.

the higher-fluence laser, resulting in a higher peak temperature and a faster ramping rate. Such annealing conditions are expected to create a larger number of nucleation sites, leading to a fine-grained structure. This difference in the grain size is consistent with the resistivity measurements in which the sample in (b) exhibited higher resistivity than the sample in (c). Figure 8(d) shows the EDS elemental maps of the 50 000-shot sample in (c) and the corresponding compositional profile along the thickness direction. There is no noticeable interdiffusion among the seed, CMFG, and cap layers. This suggests that ELA is applicable to Heusler-based multilayer devices, where interdiffusion is problematic. STEM analysis revealed no clear non-uniformity, such as grain size, along the depth direction. Although the actual temperature profile was unmeasurable, these results suggest that the effect of temperature gradient is not significant in these experiments, which can be attributed to the thermal properties of our samples. Because the sample structure consists of metallic seed, CMFG, and cap layers with high thermal conductivity and a SiO_2 underlayer with low thermal conductivity, the generated heat is confined in the CMFG layer, contributing to the uniform temperature. To actively make use of the steep temperature gradient, designing the thermal and optical properties of samples and optimizing ELA condition are required. For example, introducing a thermal barrier layer with low thermal resistivity above a low thermal-budget region and below Heusler-based device film can enhance the temperature difference between them. Additionally, incorporating a heat sink structure or reducing the laser pulse width could be explored.

IV. CONCLUSIONS

We investigated the effect of ELA as a thermal treatment for Heusler-alloy thin films because of its potential to address the temperature constraint in practical applications due to the short annealing time and temperature gradient. XRD analysis confirmed that ELA successfully transformed the as-deposited amorphous CMFG film into a polycrystalline structure with *B*2 atomic ordering, which is crucial to derive the material's potential. Although excess fluence resulted in increased surface roughness, we identified a process window, where atomic ordering is induced without increasing the roughness. Within this window, STEM and EDS analyses revealed no noticeable interdiffusion between the CMFG layer and the adjacent seed and capping layers. The high film flatness without interdiffusion in the ELA samples indicates the applicability of ELA for important applications using nanometer-scale multilayers, such as MR devices. Analysis by resistivity and AMR measurements revealed that combining a modest fluence laser with a large number of laser irradiations realizes higher annealing effects, and the optimized ELA process induced annealing effects equivalent to conventional furnace annealing at approximately 300 °C. Although depth temperature profile remains unmeasured, the nature of ELA suggests that underlying layers experience lower temperatures than the CMFG layer, implying that, under the present conditions, it is feasible to form a CMFG layer with properties equivalent to 300 °C furnace annealing on structures with low thermal budget. Together with the established advantages of the ELA process such as enhanced throughput and selective area annealing, these findings demonstrate that ELA is a promising alternative annealing technique for Heusler alloys in spintronic applications and can broaden their scope of use. However, furnace annealing at higher temperatures was found more effective than ELA under the conditions tested in this study, presumably due to the limited kinetics in the nanosecond-scale ELA process. Future work should focus on designing sample structures and materials from thermal and optical perspectives and optimizing ELA conditions to enhance the annealing effects and actively make use of the thermal gradient.

ACKNOWLEDGMENTS

This work was partially supported by Advanced Storage Research Consortium (ASRC), ARIM of MEXT (JPMXP12 25NM5220), MEXT Initiative to Establish Next-generation Novel Integrated Circuits Centers (X-NICS) (Grant No. JPJ011438), and Gigaphoton Inc. The authors thank M. Inoue of NIMS for technical support.

AUTHOR DECLARATIONS

Conflict of Interest

The authors have no conflicts to disclose.

Author Contributions

Hirofumi Suto: Conceptualization (equal); Investigation (equal); Project administration (equal); Visualization (equal); Writing – original draft (equal). **Keita Katayama:** Investigation (equal); Methodology (lead); Writing – review & editing (equal). **Yohei Tanaka:** Investigation (equal); Methodology (equal); Writing – review & editing (equal). **Dolly Taparia:** Investigation (equal). **Nattamon Suwannaharn:** Investigation (equal); Visualization (equal); Writing – original draft (equal). **Tomoya Nakatani:** Investigation (equal); Writing – review & editing (equal). **Taisuke T. Sasaki:** Investigation (equal); Writing – review & editing (equal). **Hisato Yabuta:** Conceptualization (equal); Supervision (equal); Writing – review & editing (equal). **Yuya Sakuraba:** Conceptualization (equal); Supervision (equal); Writing – review & editing (equal).

DATA AVAILABILITY

The data that support the findings of this study are available from the corresponding author upon reasonable request.

REFERENCES

[1] M. R. Page, T. M. Nakatani, D. A. Stewart, B. R. York, J. C. Read, Y. S. Choi, and J. R. Childress, "Temperature-dependence of current-perpendicular-to-the-plane giant magnetoresistance spin-valves using $Co_2(Mn_{1-x}Fe_x)Ge$ Heusler alloys," J. Appl. Phys. **119**, 2 (2016).

[2] Y.-s. Choi, T. Nakatani, J. C. Read, M. J. Carey, D. A. Stewart, and J. R. Childress, "Enhancement of current-perpendicular-to-plane giant magnetoresistance by insertion of amorphous ferromagnetic underlayer in Heusler alloy-based spin-valve structures," Appl. Phys. Express **10**, 013006 (2017).

[3] S. Li, T. Nakatani, K. Masuda, Y. Sakuraba, X. D. Xu, T. T. Sasaki, H. Tajiri, Y. Miura, T. Furubayashi, and K. Hono, "Enhancement of current-perpendicular-to-plane giant magnetoresistive outputs by improving

B2-order in polycrystalline $Co_2(Mn_{0.6}Fe_{0.4})$Ge Heusler alloy films with the insertion of amorphous CoFeBTa underlayer," Acta Mater. **142**, 49 (2018).

[4] T. Nakatani, S. Li, Y. Sakuraba, T. Furubayashi, and K. Hono, "Advanced CPP-GMR spin-valve sensors for narrow reader applications," IEEE Trans. Magn. **54**, 3300211 (2018).

[5] T. Nakatani, S. K. Narayananellore, L. S. R. Kumara, H. Tajiri, Y. Sakuraba, and K. Hono, "Thickness dependence of degree of B2 order of polycrystalline $Co_2(Mn_{0.6}Fe_{0.4})$Ge Heusler alloy films measured by anomalous x-ray diffraction and its impacts on current-perpendicular-to-plane giant magnetoresistance properties," Scr. Mater. **189**, 63 (2020).

[6] V. Barwal, H. Suto, R. Toyama, K. Simalaotao, T. Sasaki, Y. Miura, and Y. Sakuraba, "Large magnetoresistance and high spin-transfer torque efficiency of $Co_2Mn_xFe_{1-x}$Ge $(0 \leq x \leq 1)$ Heusler alloy thin films obtained by high-throughput compositional optimization using combinatorially sputtered composition-gradient film," APL Mater. **12**, 111114 (2024).

[7] S. Li, Y. K. Takahashi, T. Furubayashi, and K. Hono, "Enhancement of giant magnetoresistance by L21 ordering in $Co_2Fe(Ge_{0.5}Ga_{0.5})$ Heusler alloy current-perpendicular-to-plane pseudo spin valves," Appl. Phys. Lett. **103**, 042405 (2013).

[8] Y. Du, T. Furubayashi, T. T. Sasaki, Y. Sakuraba, Y. K. Takahashi, and K. Hono, "Large magnetoresistance in current-perpendicular-to-plane pseudo spin-valves using $Co_2Fe(Ga_{0.5}Ge_{0.5})$ Heusler alloy and AgZn spacer," Appl. Phys. Lett. **107**, 112405 (2015).

[9] J. W. Jung, Y. Sakuraba, T. T. Sasaki, Y. Miura, and K. Hono, "Enhancement of magnetoresistance by inserting thin NiAl layers at the interfaces in $Co_2FeGa_{0.5}Ge_{0.5}/Ag/Co_2FeGa_{0.5}Ge_{0.5}$ current-perpendicular-to-plane pseudo spin valves," Appl. Phys. Lett. **108**, 102408 (2016).

[10] D. Taparia *et al.*, "Improvement in CPP-GMR read head sensor performance using [001]-oriented polycrystalline half-metallic Heusler alloy $Co_2FeGa_{0.5}Ge_{0.5}$ and CoFe bilayer electrode," Sci. Technol. Adv. Mater. **25**, 2388503 (2024).

[11] Y. Sakuraba, K. Izumi, T. Iwase, S. Bosu, K. Saito, K. Takanashi, Y. Miura, K. Futatsukawa, K. Abe, and M. Shirai, "Mechanism of large magnetoresistance in $Co_2MnSi/Ag/Co_2$ MnSi devices with current perpendicular to the plane," Phys. Rev. B **82**, 094444 (2010).

[12] T. Kubota, Y. Ina, Z. Wen, H. Narisawa, and K. Takanashi, "Current perpendicular-to-plane giant magnetoresistance using an $L1_2$ Ag_3Mg spacer and $Co_2Fe_{0.4}Mn_{0.6}Si$ Heusler alloy electrodes: Spacer thickness and annealing temperature dependence," Phys. Rev. Mater. **1**, 044402 (2017).

[13] E. Vilanova Vidal, G. Stryganyuk, H. Schneider, C. Felser, and G. Jakob, "Exploring Co_2MnAl Heusler compound for anomalous Hall effect sensors," Appl. Phys. Lett. **99**, 132509 (2011).

[14] P. Li *et al.*, "Giant room temperature anomalous Hall effect and tunable topology in a ferromagnetic topological semimetal Co_2MnAl," Nat. Commun. **11**, 3476 (2020).

[15] A. Sakai *et al.*, "Giant anomalous Nernst effect and quantum-critical scaling in a ferromagnetic semimetal," Nat. Phys. **14**, 1119 (2018).

[16] K. Sumida *et al.*, "Spin-polarized Weyl cones and giant anomalous Nernst effect in ferromagnetic Heusler films," Commun. Mater. **1**, 89 (2020).

[17] G. Albuquerque, S. Hernandez, M. T. Kief, D. Mauri, and L. Wang, "HDD reader technology roadmap to an areal density of 4 Tbpsi and beyond," IEEE Trans. Magn. **58**, 1 (2022).

[18] T. Nakatani, P. D. Kulkarni, H. Suto, K. Masuda, H. Iwasaki, and Y. Sakuraba, "Perspective on nanoscale magnetic sensors using giant anomalous Hall effect in topological magnetic materials for read head application in magnetic recording," Appl. Phys. Lett. **124**, 070501 (2024).

[19] D. Edelstein *et al.*, "A 14 nm embedded STT-MRAM CMOS technology," in *Technical Digest—International Electron Devices Meeting, IEDM, Vols. 2020-December* (Institute of Electrical and Electronics Engineers Inc., 2020), pp. 11.5.1–11.5.4.

[20] L. M. Loong, W. Lee, X. Qiu, P. Yang, H. Kawai, M. Saeys, J.-H. Ahn, and H. Yang, "Flexible MgO barrier magnetic tunnel junctions," Adv. Mater. **28**, 4983 (2016).

[21] J.-Y. Chen, Y.-C. Lau, J. M. D. Coey, M. Li, and J.-P. Wang, "High performance MgO-barrier magnetic tunnel junctions for flexible and wearable spintronic applications," Sci. Rep. **7**, 42001 (2017).

[22] S. Ota, A. Ando, T. Sekitani, T. Koyama, and D. Chiba, "Flexible CoFeB/MgO-based magnetic tunnel junctions annealed at high temperature (≥350 °C)," Appl. Phys. Lett. **115**, 202401 (2019).

[23] S. Bosu, Y. Sakuraba, T. T. Sasaki, S. Li, and K. Hono, "Enhancement of L2 1 order and spin-polarization of Heusler alloy Co_2MnSi thin film by Ag alloying," Scr. Mater. **110**, 70 (2016).

[24] S. Li, Y. Sakuraba, T. Sasaki, J. Chen, S. Bosu, and K. Hono, "Enhanced current-perpendicular-to-plane giant magnetoresistance by improvement of atomic order of Co_2FeSi Heusler alloy film through Ag doping," AIP Adv. **8**, 075230 (2018).

[25] J. Chen *et al.*, "Fully epitaxial giant magnetoresistive devices with half-metallic Heusler alloy fabricated on poly-crystalline electrode using three-dimensional integration technology," Acta Mater. **200**, 1038 (2020).

[26] T. Sameshima, S. Usui, and M. Sekiya, "XeCl excimer laser annealing used in the fabrication of poly-Si TFTs," IEEE Electron Device Lett. **7**, 276 (1986).

[27] H. Watanabe, H. Miki, S. Sugai, K. Kawasaki, and T. Kioka, "Crystallization process of polycrystalline silicon by KrF excimer laser annealing," Jpn. J. Appl. Phys. **33**, 4491 (1994).

[28] M. Miyasaka and J. Stoemenos, "Excimer laser annealing of amorphous and solid-phase-crystallized silicon films," J. Appl. Phys. **86**, 5556 (1999).

[29] E. E. Marinero, "Material transformations in semiconductor and magnetic thin films," Appl. Surf. Sci. **43**, 117 (1989).

[30] S. S. N. Bharadwaja, T. Dechakupt, S. Trolier-Mckinstry, and H. Beratan, "Excimer laser crystallized $(Pb,La)(Zr,Ti)O_3$ thin films," J. Am. Ceram. Soc. **91**, 1580 (2008).

[31] L. Grenouillet *et al.*, "Nanosecond laser anneal (NLA) for Si-implanted HfO_2 ferroelectric memories integrated in back-end of line (BEOL)," in *2020 IEEE Symposium on VLSI Technology* (IEEE, 2020), pp. 1–2.

[32] T. Okuda, A. Sugimura, O. Eryu, L. K. E. B. Serrona, N. Adachi, I. Sakamoto, and A. Nakanishi, "Nd-Fe-B thin films with perpendicular magnetic anisotropy and high coercivity prepared by pulsed laser annealing," Jpn. J. Appl. Phys. **42**, 6859 (2003).

[33] M. Perzanowski, M. Krupinski, A. Zarzycki, Y. Zabila, and M. Marszalek, "Structural ordering of laser-processed FePdCu thin alloy films," J. Alloys Compd. **646**, 773 (2015).

[34] J. Nomoto, T. Koida, I. Yamaguchi, H. Makino, Y. Kitanaka, T. Nakajima, and T. Tsuchiya, "Over 130 cm^2/Vs Hall mobility of flexible transparent conductive In_2O_3 films by excimer-laser solid-phase crystallization," NPG Asia Mater. **14**, 76 (2022).

[35] S. W. Kim, S. D. Choi, D. H. Jin, K. A. Lee, S. S. Lee, and D. G. Hwang, "Local magnetization reversal in exchange biased film by laser annealing," J. Magn. Magn. Mater. **272–276**, 376–377 (2004).

[36] I. Berthold, M. Müller, S. Klötzer, R. Ebert, S. Thomas, P. Matthes, M. Albrecht, and H. Exner, "Investigation of selective realignment of the preferred magnetic direction in spin-valve layer stacks using laser radiation," Appl. Surf. Sci. **302**, 159–162 (2014).

[37] A. Sharma *et al.*, "Exchange bias and diffusion processes in laser annealed CoFeB/IrMn thin films," J. Magn. Magn. Mater. **489**, 165390 (2019).

[38] H. Kubota, J. Nakata, M. Oogane, Y. Ando, H. Kato, A. Sakuma, and T. Miyazaki, "Fabrication and characterization of Co–Mn–Al Heusler-type thin film," J. Appl. Phys. **97**, 10C913 (2005).

[39] I. A. Campbell, A. Fert, and O. Jaoul, "The spontaneous resistivity anisotropy in Ni-based alloys," J. Phys. C **3**, S95 (1970).

[40] S. Kokado, M. Tsunoda, K. Harigaya, and A. Sakuma, "Anisotropic magnetoresistance effects in Fe, Co, Ni, Fe 4N, and half-metallic ferromagnet: A systematic analysis," J. Phys. Soc. Jpn. **81**, 024705 (2012).

[41] Y. Sakuraba, S. Kokado, Y. Hirayama, T. Furubayashi, H. Sukegawa, S. Li, Y. K. Takahashi, and K. Hono, "Quantitative analysis of anisotropic

magnetoresistance in Co_2MnZ and Co_2FeZ epitaxial thin films: A facile way to investigate spin-polarization in half-metallic Heusler compounds," Appl. Phys. Lett. **104**, 172407 (2014).

[42] V. K. Kushwaha, S. Kokado, S. Kasai, Y. Miura, T. Nakatani, R. Kumara, H. Tajiri, T. Furubayashi, K. Hono, and Y. Sakuraba, "Prediction of half-metallic gap formation and Fermi level position in Co-based Heusler alloy epitaxial thin films through anisotropic magnetoresistance effect," Phys. Rev. Mater. **6**, 064411 (2022).

[43] R. Toyama, V. K. Kushwaha, T. T. Sasaki, Y. Iwasaki, T. Nakatani, and Y. Sakuraba, "Combinatorial optimization for high spin polarization in Heusler alloy composition-spread thin films by anisotropic magnetoresistance effect," APL Mater. **11**, 101127 (2023).